The PET-Tracer ^{89}Zr-Df-IAB22M2C Enables Monitoring of Intratumoral CD8 T-cell Infiltrates in Tumor-Bearing Humanized Mice after T-cell Bispecific Antibody Treatment

Christoph M. Griessinger[1], Tove Olafsen[2], Alessandro Mascioni[2], Ziyue Karen Jiang[2], Charles Zamilpa[2], Fang Jia[2], Michael Torgov[2], Jason M. Romero[2], Filippo Marchioni[2], Daulet Satpayev[2], Chenyu Lee[2], Green Zhang[2], Tapan K. Nayak[1], Mudita Pincha[3], Maria Amann[3], Preethi L.B. Mohan[3], Marine Richard[3], Valeria G. Nicolini[3], Johannes Sam[3], Christina Claus[3], Claudia Ferrara[3], Peter Brünker[3], Marina Bacac[3], Pablo Umana[3], Dominik Rüttinger[4], Ian A. Wilson[2], Jean Gudas[2], Christian Klein[3], and Jean J.L. Tessier[1]

ABSTRACT

CD8-expressing T cells are the main effector cells in cancer immunotherapy. Treatment-induced changes in intratumoral CD8$^+$ T cells may represent a biomarker to identify patients responding to cancer immunotherapy. Here, we have used a ^{89}Zr-radiolabeled human CD8-specific minibody (^{89}Zr-Df-IAB22M2C) to monitor CD8$^+$ T-cell tumor infiltrates by PET. The ability of this tracer to quantify CD8$^+$ T-cell tumor infiltrates was evaluated in preclinical studies following single-agent treatment with FOLR1-T-cell bispecific (TCB) antibody and combination therapy of CEA-TCB (RG7802) and CEA-targeted 4-1BB agonist CEA-4-1BBL. *In vitro* cytotoxicity assays with peripheral blood mononuclear cells and CEA-expressing MKN-45 gastric or FOLR1-expressing HeLa cervical cancer cells confirmed noninterference of the anti-CD8-PET-tracer with the mode of action of CEA-TCB/CEA-4-1BBL and FOLR1-TCB at relevant doses. *In vivo*, the extent of tumor regression induced by combination treatment with CEA-TCB/CEA-4-1BBL in MKN-45 tumor–bearing humanized mice correlated with intratumoral CD8$^+$ T-cell infiltration. This was detectable by ^{89}Zr-IAB22M2C-PET and γ-counting. Similarly, single-agent treatment with FOLR1-TCB induced strong CD8$^+$ T-cell infiltration in HeLa tumors, where ^{89}Zr-Df-IAB22M2C again was able to detect CD8 tumor infiltrates. CD8-IHC confirmed the PET imaging results. Taken together, the anti-CD8-minibody ^{89}Zr-Df-IAB22M2C revealed a high sensitivity for the detection of intratumoral CD8$^+$ T-cell infiltrates upon either single or combination treatment with TCB antibody–based fusion proteins. These results provide further evidence that the anti-CD8 tracer, which is currently in clinical phase II, is a promising monitoring tool for intratumoral CD8$^+$ T cells in patients treated with cancer immunotherapy.

Significance: Monitoring the pharmacodynamic activity of cancer immunotherapy with novel molecular imaging tools such as ^{89}Zr-Df-IAB22M2C for PET imaging is of prime importance to identify patients responding early to cancer immunotherapy.

Introduction

Cytotoxic CD8$^+$ T lymphocytes (CTL) are the main effector cells in clinically approved checkpoint inhibitors (CPI), and most cancer immunotherapy drugs under development (1–3). In the case of CPI, CTL are either newly recruited to the tumor or are reactivated in the tumor microenvironment (TME). CTL recognize malignant tumor cells via MHC-I and directly kill cancer cells through the release of granzyme B and perforin.

T-cell bispecific antibodies (TCB) are a new class of bispecific antibodies (bsAb) that bind to the T-cell receptor (TCR) CD3ε subunit and a tumor-associated antigen. They activate T cells independently of any TCR specificity and mediate T-cell cross-linking between CD3-expressing T cells and tumor cells, expressing the associated antigen, which results in efficient tumor cell lysis (4, 5). The concomitant release of cytokines and chemokines can recruit additional immune cells into the tumor (5). The TCBs used in these studies target carcinoembryonic antigen (CEA) and folate receptor 1 (FOLR1). Both, CEA and FOLR1 are glycophosphatidylinositol-anchored (GPI) glycoproteins. CEA is usually expressed at high levels on cells of colorectal cancer, pancreatic adenocarcinoma, gastric cancer, non–small cell lung cancer, and breast cancer and at lower levels on healthy glandular epithelia of the gastrointestinal tract (6). FOLR1, which is overexpressed on ovarian, lung, renal, and other solid malignancies, while showing a limited expression on healthy tissues, binds folic acid and mediates its intracellular uptake (7, 8).

Both CEA- and FOLR1-TCB contain P329G, L234A, and L235A mutations (P329G-LALA) in their Fc domain to reduce Fcγ-receptor

[1]Early Clinical Development Oncology, Roche Pharmaceutical Research & Early Development, Roche Innovation Center Basel, Basel, Switzerland. [2]ImaginAb Inc., Inglewood, California. [3]Roche Pharmaceutical Research & Early Development, Roche Innovation Center Zurich, Schlieren, Switzerland. [4]Early Clinical Development, Roche Pharmaceutical Research & Early Development, Roche Innovation Center Munich, Penzberg, Switzerland.

Note: Supplementary data for this article are available at Cancer Research Online (http://cancerres.aacrjournals.org/).

C.M. Griessinger and T. Olafsen contributed equally to this article.

Corresponding Authors: Jean J.L. Tessier, F. Hoffmann-La Roche Ltd., Grenzacherstrasse 124, Basel 4070, Switzerland. Phone: 416-1688-7094; E-mail: jean.tessier@roche.com; and Christoph M. Griessinger, Phone: 416-1687-3953; E-mail: christoph_michael.griessinger@roche.com

Cancer Res 2020;80:2903–13

doi: 10.1158/0008-5472.CAN-19-3269

(FcR)-mediated reactions such as antibody-dependent cellular cytotoxicity, antibody-depended cellular phagocytosis, and complement-dependent cytotoxicity, while retaining neonatal FcR binding for IgG-like pharmacokinetics (4, 9). The tumor cell lines used in these experiments included MKN-45 human gastric cancer expressing CEA, and HeLa human cervical cancer expressing FOLR1.

TCB-induced T-cell activation triggers an upregulation of costimulating receptors such as 4-1BB (CD137), a member of the TNFR superfamily. 4-1BB stimulation results in T-cell proliferation, cytotoxicity, proinflammatory Th1 polarization, and memory cell formation (10, 11). To stimulate 4-1BB signaling, we used CEA-4-1BBL, which is a novel bsAb-based fusion protein that contains a split, trimeric 4-1BB-ligand moiety, and a binding arm for CEA. The Fc domain of this CEA-4-1BBL is also effector function silent (P329G-LALA mutation; refs. 12, 13). The combination therapy of tumor-associated antigen-targeted TCB and tumor-targeted 4-1BBL induces a strong expansion of CTLs that has been shown to induce profound antitumor activity in various preclinical solid and lymphoma tumor models (14). The use of TCB combination therapies can be considered as an off-the-shelf alternative to adoptive transfer of chimeric antigen receptor T cells (15).

The development of immunotherapy is transforming cancer treatments for many solid tumors and hematologic malignancies. Unfortunately, many patients do not benefit from these drugs and there is currently a lack of tools that can be used to accurately predict which patients may benefit from treatment. In the case of clinical imaging, traditional tumor assessment criteria are often confounded by the inability to distinguish true tumor progression from pseudoprogression; the increase in tumor mass associated with immune cell infiltration. To overcome the limitations of current tumor imaging assessments, a new class of imaging agents is being developed to monitor and quantify immune cell populations *in vivo*, longitudinally and throughout the body (16). This is the case for PET, for which tracers are being designed using either conventional full length antibodies, small peptides, antibody fragments such as minibodies, diabodies, nanobodies, or engineered proteins such as affibodies or adnectins, that bind specific epitopes on immune cell epitopes (16–18). CD8, which is expressed on CTLs, is an antigen that is highly suitable as a target for immune cell–specific tracers.

The humanized CD8α-chain–specific minibody (Mb), ^{89}Zr-Df-IAB22M2C, which is currently in clinical development, consists of two V_H/V_L chains containing the complementarity determining regions for CD8α, fused to a human IgG CH3 constant domain via a hinge region (19). To enable radiolabeling for PET, the Mb is conjugated to the chelator desferrioxamine (Df), which allows radiolabeling with the positron-emitting radioisotope Zirconium-89 (^{89}Zr; half-life: 3.3 days). The lack of CH1 and CH2 domains makes the Mb inert for any FcRγ-mediated reactions. The Mb has the same specificity for CD8 as the parental full-length mAb, but due to its reduced size of approximately 80 kDa, it overcomes some of the limitations of a full-length mAb (∼150 kDa). The smaller Mb format exhibits (i) a reduced plasma half-life, resulting in lower background signals in target tissues due to faster clearance, (ii) a higher tissue penetration, especially in the tumor, and (iii) reduced immunogenicity. Data from the first clinical trials using the anti-CD8 Mb, demonstrated targeting of tumors and CD8-rich tissues, favorable pharmacokinetics, and no side effects after injection (19). To date, monitoring treatment response with ^{89}Zr-Df-IAB22M2C-PET during cancer immunotherapy has not been reported.

Here, we investigated whether the radiolabeled humanized CD8-specific Mb, ^{89}Zr-Df-IAB22M2C, is capable of detecting and quantifying CD8$^+$ T-cell infiltrates in two cancer immunotherapy regimens in tumor-bearing humanized mice: (i) after combination therapy of CEA-TCB with CEA-4-1BBL and (ii) after FOLR1-TCB monotherapy.

Material and Methods

Experimental animals

Humanized CD34$^+$ stem cell engrafted NOD SCID gamma (NSG) mice were purchased from Jackson Laboratory and housed and maintained by the Department of Laboratory Animal Medicine at the University of California, Los Angeles (UCLA; Los Angeles, CA). Animals were acquired 14–16 weeks after the stem cell transfer when the percentage of human CD45$^+$ cells in blood was >25%. The animal studies were approved by the Chancellor's Animal Research Committee at UCLA (Institutional Animal Care and Use Committee protocol compliant) and conducted in accordance with institutional guidelines and protocols.

Therapeutic molecules and human tumor cell lines

Human-specific CEA-4-1BBL, CEA-TCB, and FOLR1-TCB were engineered by Roche Innovation Center Zürich. All molecules were freshly diluted from stock prior to use.

Human-derived MKN-45 gastric cancer cells (DSMZ) were cultured in 90% DMEM (Thermo Fisher Scientific) and 10% heat-inactivated FBS (Thermo Fisher Scientific) with 2–3 cell passage per week. HeLa human cervical cancer cells (ATCC) were cultured in RPMI1640 (Thermo Fisher Scientific) with 10% heat-inactivated FBS (Thermo Fisher Scientific) and passaged two/three times per week. The tumor cells were tested for *Mycoplasma* using the Stat-Myco Test (Idexx Bioanalytics).

Tumor engraftment and cancer immunotherapy with CEA-TCB/CEA-4-1BBL combination or FOLR1-TCB therapy

For the CEA-TCB/CEA-4-1BBL combination study, we injected 1×10^6 MKN-45 cells in a volume of 100 μL at a 1:1 ratio of RPMI and Matrigel (BD Biosciences). The cell suspension was injected subcutaneously in the right flank of the experimental mice using a 28 G needle. The tumor volume was monitored 2–3 times per week by caliper measurements and calculated by the formula: tumor volume = $0.52 \times \text{length} \times \text{width}^2$. Twenty days after tumor engraftment, when the tumor volumes were approximately 200 mm^3, experimental animals were randomized and allocated to treatment groups. The CEA-TCB/CEA-4-1BBL combination treatment group received CEA-TCB twice weekly (Tuesday and Friday) at a concentration of 2.5 mg/kg and CEA-4-1BBL at 3 mg/kg once weekly (Friday) by intraperitoneal injection in a volume of 200 μL. CEA-TCB and CEA-4-1BBL single treatment was performed at the same concentration twice weekly for CEA-TCB and once weekly for CEA-4-1BBL. Also, once a week, the control group was treated with 200 μL histidine buffer (20 mmol/L Histidine, 140 mmol/L NaCl, pH 6.0) by intraperitoneal treatment.

For the FOLR1-TCB study, 5×10^6 HeLa cells were also engrafted subcutaneously in a 1:1 mixture of RPMI and Matrigel in a volume of 100 μL into the right flank of the experimental mice using a 28 G needle. Tumor volume was monitored twice a week using a caliper. When the tumor reached the size of approximately 150 mm^3 after 35 days, the animals were randomized into treatment groups and received two intraperitoneal injections of 200 μL FOLR1-TCB at a concentration of 2 mg/kg or vehicle (i.e., histidine buffer) 3 days apart (days 0 and 3).

In vivo PET imaging

For the CEA-4-1BBL/CEA-TCB study, mice were injected intravenously with 54.4 ± 1.7 μCi (∼10 μg) of ^{89}Zr-Df-IAB22M2C 3 days after the last treatment. Two days after the last FOLR1-TCB treatment, the experimental mice were injected intravenously with 95.3 ± 2.2 μCi (∼10 μg) of ^{89}Zr-Df-IAB22M2C. The animals were scanned in SofieBiosciences G8 PET/CT Imaging System (PerkinElmer) 40 hours after injection of the radiolabeled Mb. Static PET scans with 10 minutes duration were acquired with an energy range set to 150–650 keV and CT scans were acquired with x-ray sources set to 50 kVp and 200 μA. The PET/CT scans were reconstructed using a three-dimensional maximum likelihood estimation method reconstruction spread across 32 central processing units. All reconstructed PET/CT images were analyzed by Medical Image Data Examiner (AMIDE) software (20) or Vivoquant (InviCRO LLC) and presented as maximum intensity projections (MIP). To analyze the PET scans, 3D regions of interest (ROI) were place on the organs of interest and the %ID/cc was calculated.

Results

The anti-CD8-Mb IAB22M2C and CEA-TCB/CEA-4-1BBL or FOLR1-TCB do not interfere *in vitro*

To determine whether CD8 coreceptor occupancy with the anti-CD8 Mb might affect the activity of TCB-mediated TCR cross-linking, activation, and subsequent tumor cell killing, an imaging-based *in vitro* cytotoxicity assay was conducted. This assay has the advantage of monitoring kinetics of tumor cell death over time, and directly measures tumor cell apoptosis using Caspase 3/7 apoptosis dye. In the clinical practice, the anti-CD8 Mb will be rather used after administration of the drug, most preferentially at the time when response to therapeutic treatment is commencing and immune cell infiltration is occurring. To reflect this, the anti-CD8 Mb was added 5 hours after initiation of the TCB-mediated cytotoxicity assay, at the saturating concentration of 125 nmol/L (2 μg/200 μL/well = 10 μg/mL).

Tumor cell killing was measured by plotting tumor cell count over time and calculating the corresponding AUC. Addition of the anti-CD8 Mb, IAB22M2C, had no effect on MKN-45-NLR tumor cell killing mediated by peripheral blood mononuclear cells (PBMC) treated with combination of CEA-TCB and CEA-4-1BBL (**Fig. 1A**). During the 5-hour period prior to the addition of anti-CD8 Mb, no induction of apoptosis was detected. Conversely, a sharp increase of apoptotic tumor cells was observed 20 hours post-initiation of the assay (**Fig. 1B**). The true percentage of tumor cell lysis, determined by normalizing AUC values to the untreated control, confirmed the results (Supplementary Fig. S1A and S1B).

To verify that our findings were irrespective of the tumor antigen or the TCB used, we tested the FOLR1-expressing tumor cell line HeLa-NLR. Hela-NLR cells expressing FOLR1 were cocultured with PBMCs in the presence of FOLR1-TCB. During the first 5 hours of the assay before IAB22M2C was added to the cell culture no apoptosis induction was detected. An increase of apoptotic tumor cells was, however, observed 10 hours post-initiation of the FOLR1-TCB assay (**Fig. 1D**). The presence of IAB22M2C did not affect tumor cell killing at high TCB concentrations (10 nmol/L to 80 pmol/L; **Fig. 1C**). At extremely low doses of TCB treatment, where the amount of IAB22M2C was up to 8,000-fold higher than the FOLR1-TCB concentration (16–0.64 pmol/L), tumor cell killing was significantly reduced as indicated by the AUC. Using the true percentage of tumor cell lysis, determined as explained above, these differences were only observable at 0.64 pmol/L concentration of FOLR1-TCB (Supplementary Fig. S1C and S1D).

^{89}Zr-Df-IAB22M2C is able to monitor T-cell infiltration upon CEA-TCB/CEA-4-1BBL treatment

The ability of the human radiolabeled anti-CD8-Mb, ^{89}Zr-Df-IAB22M2C, to monitor CD8$^+$ T-cell infiltration during therapy with CEA-TCB/CEA-4-1BBL was evaluated in the MKN-45 human gastric cancer implanted in humanized mice (14). For this purpose, humanized mice carrying MKN-45 gastric cancer xenografts were treated for 2 weeks with either histidine buffer as vehicle, 2.5 mg/kg CEA-TCB twice weekly, 3 mg/kg CEA-4-1BBL once weekly, or a combination of both compounds at the same concentrations and administration frequency (**Fig. 2A**). Three days after the last treatment, the anti-CD8-Mb, ^{89}Zr-Df-IAB22M2C, was injected and PET/CT was performed after 40 hours (**Fig. 2A**).

Tumor growth curves revealed strong tumor regression in the animals after combination therapy with CEA-TCB and CEA-4-1BBL. Administration of single-agent CEA-TCB or CEA-4-1BBL treatments induced antitumoral responses, which were clearly lower compared with the combination therapy (**Fig. 2B**).

Treatment-related CD8$^+$ T-cell infiltration was detected and quantified by PET imaging and γ-counting following administration of ^{89}Zr-Df-IAB22M2C (**Figs. 2C** and **3A** and **C**; Supplementary Fig. S2). In the vehicle group, low uptake (PET: 3.91 ± 0.10 %ID/cc; γ-counting: 4.87 ± 0.44 %ID/g) of ^{89}Zr-Df-IAB22M2C was detected at the tumor rim with no uptake in the tumor center. The signal at the tumor rim was presumably caused by leaky tumor vasculature, resulting in enhanced permeability, and retention, which is considered unspecific as observed in previous studies (21).

In the CEA-4-1BBL monotherapy group, individual hot spots at the tumor rims were detected and the quantification revealed an uptake of 4.07 ± 0.16 %ID/cc (PET) and 5.92 ± 0.48 %ID/g (γ-counting), respectively.

In the CEA-TCB monotherapy group, an even higher average uptake was detectable compared with the vehicle group (PET: 4.54 ± 0.23 %ID/cc; γ-counting: 6.91 ± 0.51 %ID/g; $P = 0.008$). In this group, the uptake at the tumor rim was more homogenous compared with that observed in the anti-CEA-4-1-BBL single-agent treatment group.

The highest uptake of ^{89}Zr-Df-IAB22M2C was observed in the CEA-4-1BBL and CEA-TCB combination treatment group. In this group, the tracer was homogenously distributed at the tumor rim but also present within the tumor centers. Quantification by PET and γ-counting revealed a significantly higher uptake of 5.13 ± 0.30 %ID/cc (PET) and 8.95 ± 1.60 %ID/g (γ-counting) compared with the vehicle group (PET: $P = 0.0017$; γ-counting: $P = 0.0002$) and to the CEA-4-1BBL group (PET: $P = 0.0071$; γ-counting: $P = 0.0028$). These PET and γ-counting results were further confirmed by autoradiography, which showed the spatial distribution of the ^{89}Zr-Df-IAB22M2C in the tumor after the various treatments (Supplementary Fig. S3).

Besides tumor tissue, ^{89}Zr-Df-IAB22M2C uptake was also observed in the spleen as the main CD8 T-cell sink due to its function as secondary lymphoid organ, and in the clearance organs liver and kidneys (**Figs. 2C** and **3B** and **D**; Supplementary Fig. S2). All other investigated tissues and organs such as heart, lungs, stomach, intestine, bone, carcass, and muscle as well as blood, showed very low uptake of ^{89}Zr-Df-IAB22M2C across all treatment groups. No significant differences, besides the tumors, were observed between the treatment groups throughout the examined organs and tissues.

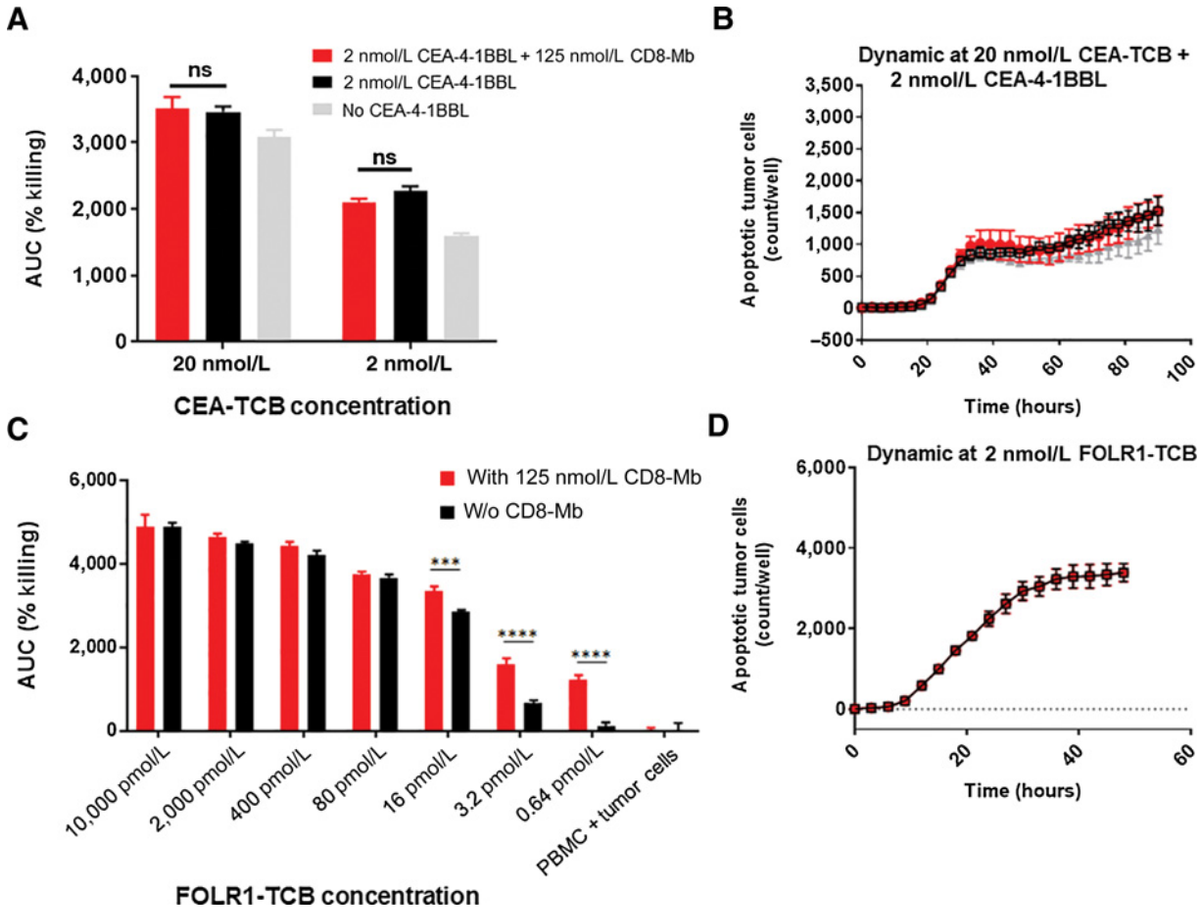

Figure 1.

In vitro cytotoxicity mediated by CEA-TCB (and CEA-4–1BBL combination treatment) or FOLR1-TCB in presence of the CD8-Mb IAB22M2C. **A** and **B,** AUC quantification (**A**) and dynamic of tumor cell lysis (based on tumor cell counts; **B**) per treatment group over time [groups with and without 125 nmol/L IAB22M2C (CD8-Mb) were treated with 2 nmol/L CEA-4-1BBL; mean ± SD; $n = 3$]. No effect of IAB22M2C was observed on tumor cell killing after treatment with CEA-TCB/CEA-4-1BBL. **C** and **D,** AUC quantification (**C**) and dynamic of tumor cell lysis (based on tumor cell counts; **D**) in groups treated with FOLR1-TCB with or without 125 nmol/L IAB22M2C ($n = 3$; mean ± SD; statistics: two-way ANOVA). At higher concentrations of FOLR1-TCB ≥ 80 pmol/L, no influence on tumor cell killing was observed in presence of IAB22M2C. ***, $P < 0.001$; ****, $P < 0.0001$; ns, not significant.

Anti-CD8-IHC staining on formalin-fixed and paraffin-embedded tumor tissue was conducted, which confirmed the *in vivo* PET and *ex vivo* γ-counting results (**Fig. 3E** and **F**). $CD8^+$ cells could be detected exclusively at the tumor rim in both the vehicle-treated (2.17 ± 0.72 $CD8^+$ cells/mm^2) and the CEA-4-1BBL- (28.58 ± 21.87 $CD8^+$ cells/mm^2) treated groups. The CEA-TCB–treated group showed a significant increase of $CD8^+$ cells over the vehicle group (212.00 ± 88.60 $CD8^+$ cells/mm^2), which were also mainly located at the tumor rim. The CEA-TCB/CEA-4-1BBL combination treatment group had the highest concentration of $CD8^+$ cells in the tumor center and at the tumor rim (566.21 ± 309.19 $CD8^+$ cells/mm^2), resulting in a significant 259-fold increase over the vehicle group.

In histologic examinations, tumor density and necrosis were assessed by hematoxylin and eosin (H&E) staining and CEA-IHC. Blood vessel formation was investigated by CD31-IHC. CEA-IHC and H&E revealed no difference in tumor density and tumor necrosis between the treatment groups, independent of tumor size (Supplementary Fig. S4A). CD31 staining and quantification revealed no significant differences in blood vessel formation regardless of the treatment administered. A slight increased frequency of small blood vessels (0–250 μm) in vehicle-treated tumors was observed, which may contribute to the unspecific background of ^{89}Zr-Df-IAB22M2C in PET and γ-counting (Supplementary Fig. S4B and S4C).

To summarize, the CD8-specific Mb ^{89}Zr-Df-IAB22M2C was capable of detecting differences in the $CD8^+$ infiltrates in MKN-45 tumors induced by mono- and combination therapy with CEA-4-1BBL and CEA-TCB as confirmed by anti-CD8-IHC *ex vivo*.

^{89}Zr-Df-IAB22M2C is able to detect intratumoral T-cell infiltrates after FOLR1-TCB treatment

Similar to the CEA-TCB/CEA-4-1BBL combination therapy, ^{89}Zr-Df-IAB22M2C PET tracer detected $CD8^+$ T cells infiltration following two doses of single-agent FOLR1-TCB in humanized mice bearing the HeLa cervical cancer model. For this purpose, huNSG mice carrying HeLa xenografts were treated with two injections of 2.0 mg/kg FOLR1-TCB 3 days apart (**Fig. 4A**). Two days later ^{89}Zr-Df-IAB22M2C was injected and PET/CT was performed 40 hours post-injection. Localization of ^{89}Zr-Df-IAB22M2C was confirmed by γ-counting and CD8-IHC.

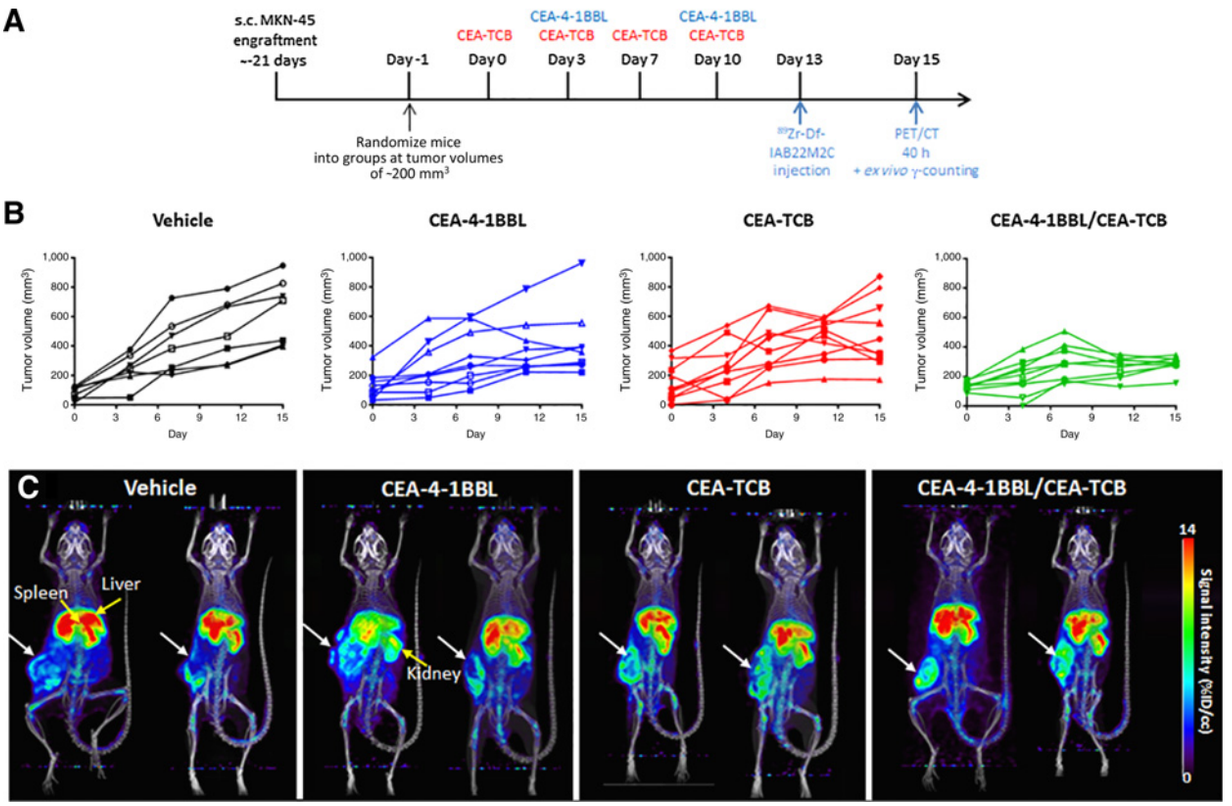

Figure 2.

Imaging CD8 T-cell infiltration upon CEA-4-1BBL/CEA-TCB mono- and combination therapy with ^{89}Zr-Df-IAB22M2C PET. **A,** Experimental layout showing the treatment protocol and imaging time points. **B,** Tumor growth curves upon treatment with vehicle/histidine buffer ($n = 7$), CEA-4-1BBL ($n = 9$), CEA-TCB ($n = 10$), and CEA-4-1BBL/CEA-TCB combination ($n = 8$). CEA-4-1BBL and CEA-TCB monotherapy showed an equal antitumoral effect, while the combination therapy with CEA-4-1BBL and CEA-TCB induced the strongest tumor regression in each experimental animal. **C,** Representative PET/CT MIP images 40 hours post-injection of ^{89}Zr-Df-IAB22M2C into mice treated with vehicle, CEA-4-1BBL, CEA-TCB mono-, and combination therapy. Two representative mice are depicted per treatment group. White arrows, the tumor; orange arrows, organs with highest uptake. Vehicle- and CEA-4-1BBL–treated groups showed sporadic circular PET signals at the tumor borders, while in CEA-TCB–treated tumors, these signals were homogenous throughout the tumor borders. In the CEA-4-1BBL/CEA-TCB–treated group the PET signals were also homogenously distributed in the center of the tumors. s.c., subcutaneous.

Two treatments with FOLR1-TCB resulted in significantly lower tumor volumes (80.88 ± 17.71 mm^3; $P = 0.0066$) as compared with vehicle treatment (189.90 ± 13.21 mm^3; **Fig. 4B**).

PET imaging with ^{89}Zr-Df-IAB22M2C revealed a low intratumoral uptake for the vehicle-treated group (3.62 ± 0.39 %ID/g) with low uptake at the tumor rim and 5.55 ± 0.50 %ID/g as determined by *ex vivo* γ-counting. In contrast, FOLR1-TCB treatment induced a significantly higher tumor uptake (PET: 6.22 ± 0.48 %ID/cc, $P = 0.0018$; γ-counting 13.63 ± 0.97 %ID/g, $P < 0.0001$ vs. vehicle), which was homogenously distributed throughout the tumor mass (**Fig. 4C** and **D**). In 4 of 8 animals, a strong uptake of the tracer was detectable in the tumor center (Supplementary Fig. S5).

Besides the tumor uptake observed by PET and γ-counting, the highest ^{89}Zr-Df-IAB22M2C uptake was detected in the spleen, liver, and kidneys, whereas there was almost no residual activity in the blood at 40 hours post-injection (**Fig. 5A** and **B**). A significantly higher uptake of ^{89}Zr-Df-IAB22M2C was observed in the spleen after FOLR1-TCB treatment (PET: 13.18 ± 0.66 %ID/cc, $P = 0.0009$; γ-counting: 41.59 ± 3.57 %ID/g, $P = 0.012$) compared with the vehicle group (PET: 9.23 ± 0.55 %ID/cc; γ-counting: 23.46 ± 5.27 %ID/g). The remaining tissues including heart, bone, and muscle showed low uptake of ^{89}Zr-Df-IAB22M2C.

CD8-IHC revealed a significant increase of CD8 cell recruitment to the tumor after FOLR1-TCB treatment (1344.17 ± 178.74 CD8$^+$ cells/mm^2; $P = 0.0086$) as compared with vehicle treatment (134.00 ± 48.11 CD8$^+$ cells/mm^2). In-line with the PET imaging results, the CD8$^+$ cells were mainly located in the tumor center after FOLR1-TCB treatment (**Fig. 5C** and **D**).

We have demonstrated that two administrations of FOLR1-TCB 3 days apart were able to induce high CD8$^+$ T-cell infiltrates in HeLa tumors, which were efficiently detected by the ^{89}Zr-Df-IAB22M2C PET tracer and confirmed by γ-counting and CD8-IHC.

Both studies, CEA-4-1BBL/CEA-TCB and FOLR1-TCB were included in a correlation to compare the *in vivo* PET/*ex vivo* γ-counting results with CD8-IHC. A positive correlation between CD8-IHC and γ-counting ($R^2 = 0.6843$) was observed (Supplementary Fig. S6A). A weaker correlation was obtained with PET ($R^2 = 0.3251$; Supplementary Fig. S6B).

Discussion

Monitoring the dynamics of tumor-infiltrating CD8$^+$ T cells using immune cell–specific tracers for PET clinical imaging, like ^{89}Zr-Df-IAB22M2C, has the potential to both transform diagnosis and staging

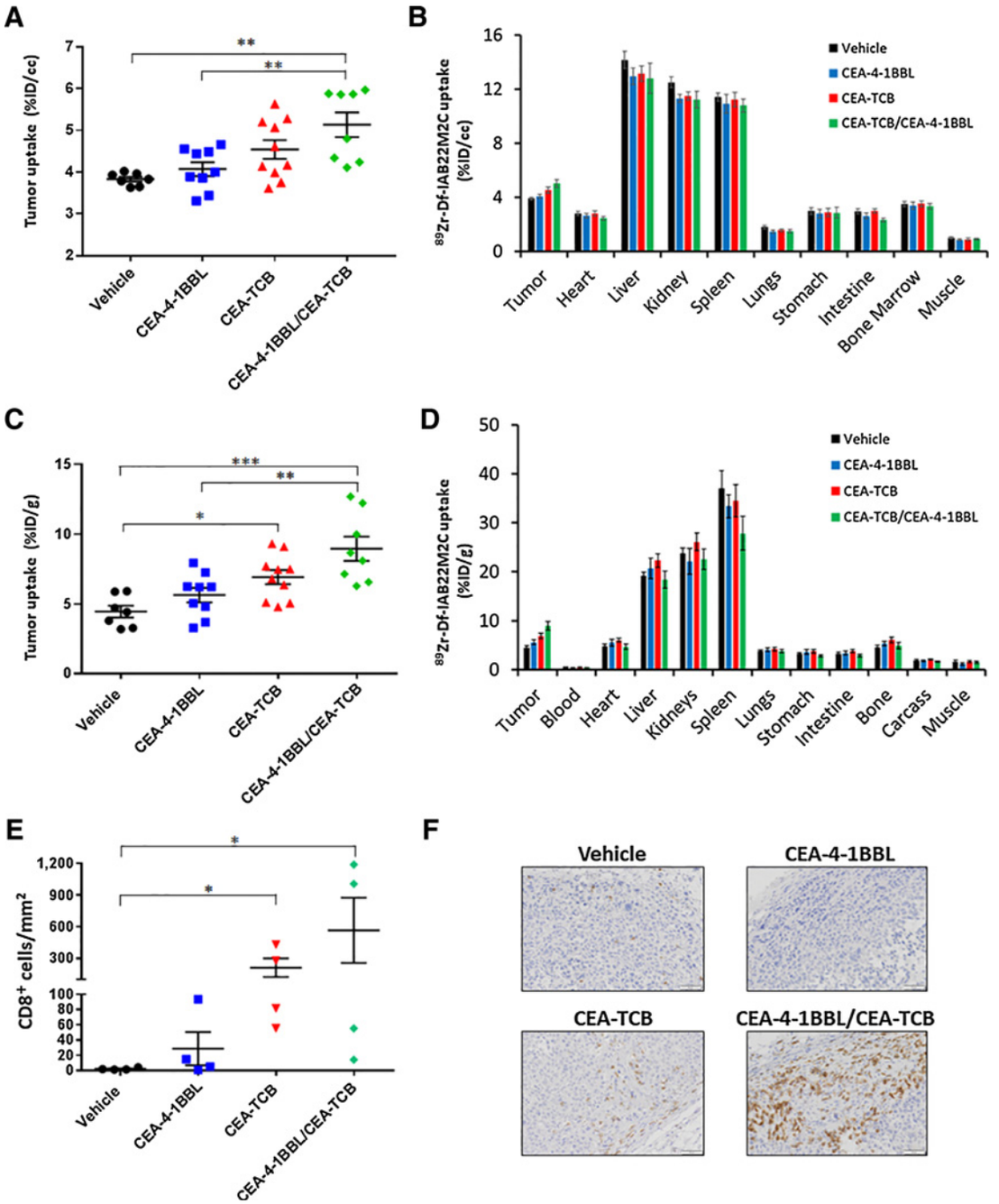

Figure 3.

Ex vivo validation of ^{89}Zr-Df-IAB22M2C PET following CEA-4-1BBL/CEA-TCB treatment by *ex vivo* γ-counting and CD8-IHC. **A,** PET analysis shows the ^{89}Zr-Df-IAB22M2C uptake (mean ± SEM; %ID/cc) in vehicle- ($n = 7$), CEA-4-1BBL- ($n = 9$), CEA-TCB- ($n = 10$), and combination-treated tumors ($n = 8$). The lowest tumor uptake was recorded for the vehicle-treated group, followed by CEA-4-1BBL and CEA-TCB monotherapy, and the highest tumor uptake was observed in the combination treatment group. Tukey Kramer, **, $P < 0.01$. **B,** Whole-body biodistribution of ^{89}Zr-Df-IAB22M2C determined by PET at 40 hours in various organs, secondary lymphoid organs, and various tissues (mean ± SEM; %ID/cc). No significant differences were observed in any organ or tissue. The highest uptake of ^{89}Zr-Df-IAB22M2 was recorded in the spleen, liver, and kidneys. **C** and **D,** γ-Counting of the tumor (**C**) and whole-body biodistribution (**D**) show the ^{89}Zr-Df-IAB22M2C uptake (mean ± SEM; %ID/g) in the different treatment groups and confirm the *in vivo* PET results. Tukey Kramer, *, $P < 0.05$; **, $P < 0.01$; ***, $P < 0.001$. **E** and **F,** CD8-IHC quantification (mean ± SEM; CD8$^+$ cells/mm^2; **E**) and representative images (**F**) from each treatment group ($n = 4$). CD8-IHC results are in-line with the γ-counting results, where the combination therapy induced the highest CD8$^+$ cell infiltrate, followed by CEA-TCB and CEA-4-1BBL monotherapies. Fishers LSD, *, $P < 0.05$.

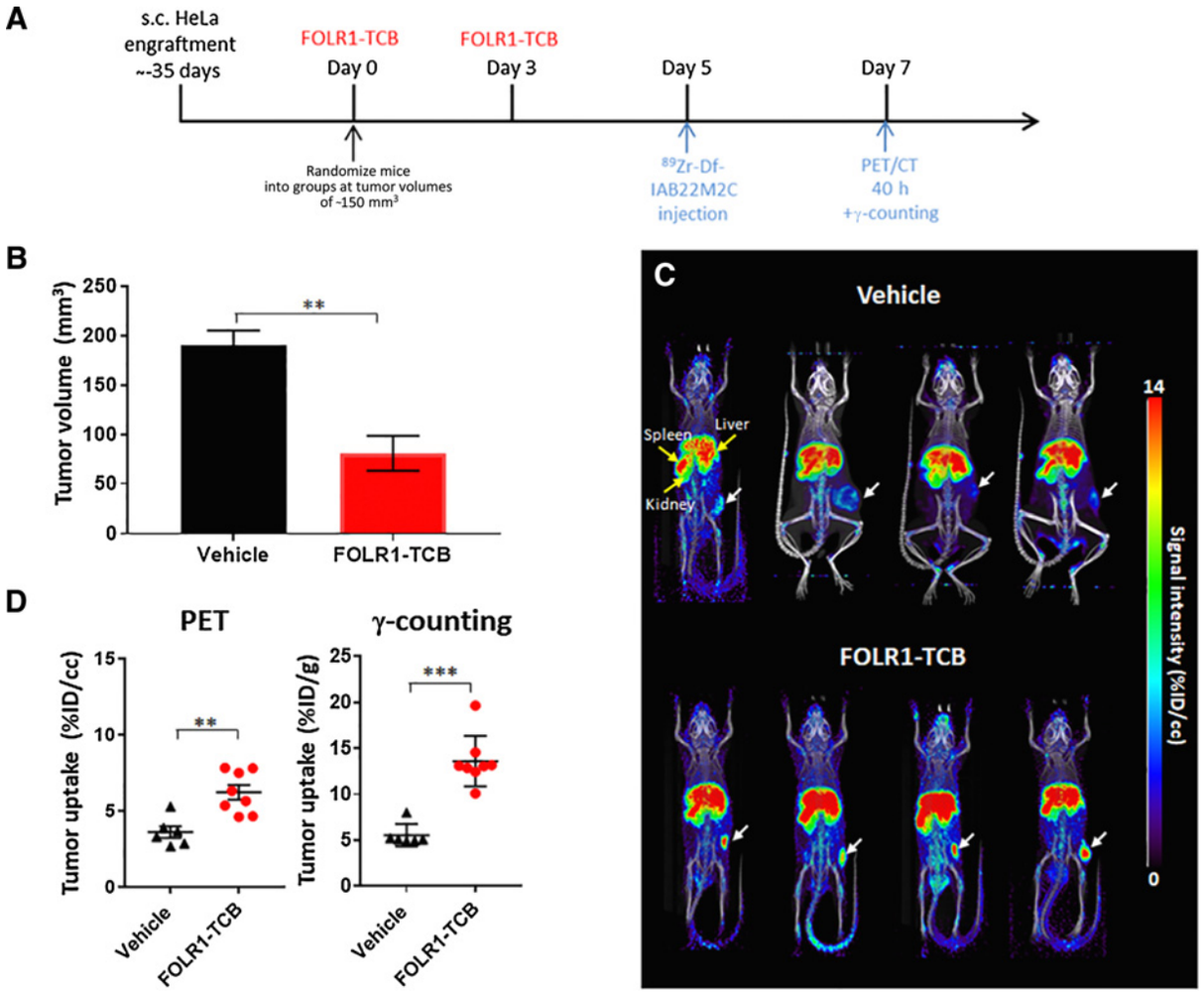

Figure 4.

Imaging CD8 T-cell infiltration upon treatment with FOLR1-TCB. **A,** Experimental layout showing the treatment schedule and imaging timepoints. **B,** Tumor volume on day 4, after two vehicle or FOLR1-TCB treatments (mean ± SEM; mm^3). Student *t* test, **, $P < 0.01$. **C,** Representative PET MIP and CT images for anatomic reference 40 hours post-injection of ^{89}Zr-Df-IAB22M2C into mice treated with vehicle or FOLR1-TCB. Four representative mice are depicted from each group. White arrows, uptake in tumor; orange arrows, uptake in organs. PET signals in the tumors after FOLR1-TCB treatment were higher compared with the vehicle treatment. **D,** PET analysis (mean ± SEM; %ID/cc) and γ-counting of tumors (mean ± SEM; %ID/g) after treatment with vehicle ($n = 6$) or FOLR1-TCB ($n = 8$). Treatment with FOLR1-TCB induced a higher uptake of ^{89}Zr-Df-IAB22M2C in HeLa tumors compared with the vehicle group. Student *t* test, **, $P < 0.01$; ***, $P < 0.001$. s.c., subcutaneous.

of patients with cancer and accelerate the development of novel cancer immunotherapy therapeutic approaches: (i) inform on patient selection (and stratification in clinical trials) based on presence of $CD8^+$ T cells in the TME, (ii) predict response to treatment early after initiation, (iii) monitor changes in T-cell infiltrates after cancer immunotherapy combination protocols and support therapeutic decision making such as, change in therapy or termination of treatment, and (iv) assess the mode of action (MoA) of new cancer immunotherapy drugs, accelerate their development, and help in defining the optimal biological/therapeutic dose for agonistic drugs.

In the preclinical studies shown here, we aimed to validate this concept by using the anti-CD8 ^{89}Zr-Df-IAB22M2C tracer following treatment with three bispecific biologics. We investigated cancer immunotherapy compounds, which have a different, agonistic MoA compared with current standard of care CPI. CEA-TCB (RG7802) is a potent T-cell activator currently under clinical development as treatment for CEA-expressing tumors (3, 4). The sister molecule of CEA-4-1BBL, fibroblast activation protein (FAP)-targeted FAP-4-1BBL (RG7826; ref. 14), is currently under development in clinical phase I trials.

First, we showed that using an *in vitro* cytotoxicity assay the administration of the CD8-Mb IAB22M2C to CEA-4-1BBL/CEA-TCB or FOLR1-TCB does not interfere with the therapeutic effect. The exclusion of any interaction between the CD8-Mb and the cancer immunotherapy drugs is essential for a potential clinical application of CD8-PET. We observed low-level tumor cell killing when cells were incubated with very low concentrations of FOLR1-TCB in the presence of an extremely high dose of anti-CD8 Mb (≥7,800-fold higher). One hypothesis for this finding is steric hindrance between the two compounds, although the two molecules are

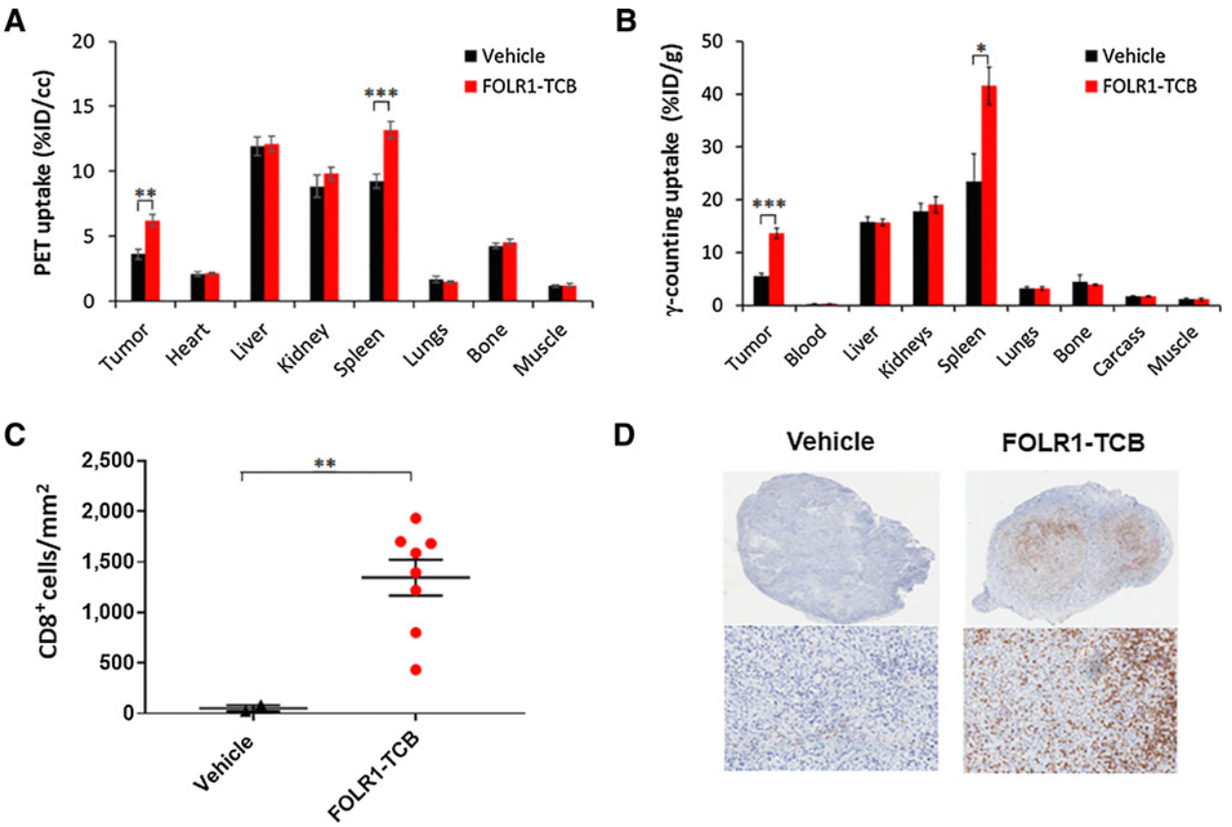

Figure 5.

Ex vivo validation of the ^{89}Zr-Df-IAB22M2C PET upon treatment with FOLR1-TCB by *ex vivo* γ-counting and CD8-IHC. **A** and **B,** PET analysis (mean ± SEM %ID/g; **A**) and γ-counting (mean ± SEM; %ID/g; **B**) of ^{89}Zr-Df-IAB22M2C whole-body biodistribution in various organs, secondary lymphoid organs, and various tissues. Only in the spleen was a significantly higher uptake of ^{89}Zr-Df-IAB22M2C observed after FOLR1-TCB treatment compared with the vehicle group. Other organs with ^{89}Zr-Df-IAB22M2 uptake were liver and kidneys. **C** and **D,** Quantification (mean ± SEM; CD8$^+$ cells/mm^2; **C**) and representative images of CD8-IHC upon vehicle ($n = 6$) and FOLR1-TCB treatment ($n = 8$; **D**). FOLR1-TCB induced a higher level of CD8$^+$ T-cell infiltrate compared with the vehicle control. Student *t* test, *, $P < 0.05$; **, $P < 0.01$; ***, $P < 0.001$.

targeting very different epitopes. However, such a high amount of anti-CD8 Mb greatly exceeds the value expected in the *in vivo* situation. As a matter of fact, in our preclinical studies, the cancer immunotherapy compounds always exceeded the amount of anti-CD8-Mb (estimated anti-CD8-Mb/FOLR1-TCB ratio to be 0.2, i.e., 40,000-times lower than the ratio needed to detect an interaction *in vitro*).

The combination of CEA-TCB and CEA-4-1BBL induced the highest tumor regression *in vivo*, with lower antitumor activity when the agents were administered as monotherapy. An antitumor effect was not expected for CEA-4-1BBL on its own, as humanized mouse models have a limited ability to provide signal 1 (activation following antigen recognition by TCR; refs. 22–24), resulting in less downstream effects such as upregulation of 4-1BB and other costimulatory receptors. As previously reported, FAP-4-1BBL or CD19-4-1BBL monotherapy had only very limited effect on tumor growth and tumoral T-cell accumulation (14). Humanized mice are complex animal models to establish and are known to be associated with development of graft-versus-host disease (25). We hypothesize that the observed antitumoral response in the CEA-4-1BBL monotherapy cohort could be a result of a mild existing allograft reaction of the humanized immune system against the MKN-45 tumors, which is intensified by the administration of CEA-4-1BBL. Because the CD34$^+$ stem cells that were transferred in the NSG mice have a different HLA composition compared with the MKN-45 tumors, an allograft reaction against the tumor is possible (25). This assumption is supported by a study of Sanmamed and colleagues, where the treatment with the anti-4-1BB–specific mAb urelumab was able to induce a potent antitumoral response in tumor-bearing humanized mice (26).

The mono- and combination therapies with CEA-TCB/CEA-4-1BBL induced varying levels of CD8$^+$ T-cell infiltrates *in vivo*, which correlate well with previously reported results (14). These differences could be visualized and quantified using the anti-CD8 Mb. IHC analysis for tumor density, necrosis, and blood vessel formation in MKN45 tumors showed no major differences between the CEA-4-1BBL/CEA-TCB mono/combination treatment groups and the vehicle group. This suggests that the unspecific background signal is present in all treatment groups, including the vehicle group, at an equal level and that the detected differences are CD8-related signals. On the basis of the PET imaging results, we were also able to detect the location of the T cells within the TME, where the monotherapy recruited T cells mainly to the tumor rim, while the combination therapy led to T-cell infiltration in the tumor rim and center. These findings are well in-line with the findings by Rashadian and colleagues, where CD8-specific nanobodies were used to detect CD8$^+$ T cells after cancer immunotherapy. With this technique the authors were able to spatially map the T-cell infiltration within the TME (27). For the second preclinical

study, we administered the very potent FOLR1-TCB bsAb, which induced strong T-cell infiltrates as detected by ^{89}Zr-Df-IAB22M2C and confirmed with CD8 IHC. In addition, the treatment with FOLR1-TCB induced an increase of ^{89}Zr-Df-IAB22M2C uptake in the spleen as compared with vehicle-treated mice, as detected in the PET images and by γ-counting. The increased uptake in the spleen was not observed in other investigated organs. Presumably, this expansion of CD8$^+$ cells is an unexpected nontumor-specific effect caused by the short and intense treatment with FOLR1-TCB. Because it was not observed after treatment with the more potent CEA-TCB and CEA-4-1BBL combination, we conclude that it might be exclusive to the FOLR1-TCB therapy regimen in HeLa-bearing humanized mice.

These studies are in agreement with preclinical results previously published with a mouse CD8-specific Mb/Db after anti-PD-1 mAb and anti-4-1BB mAb treatment (21, 28, 29). To our knowledge, the work presented here is the first reported data using a clinical human CD8-specific tracer to monitor the pharmacodynamic efficacy of TCB antibodies.

Higher CD8-IHC corresponds to higher values for both PET and γ-counting. As expected, a better correlation was observed with *ex vivo* γ-counting. PET quantification was obtained by selecting a ROI over the tumor region. This tumor region defined on the images does not match perfectly with the excised specimen collected for IHC and γ-counting. Furthermore, PET quantification was influenced by partial volume effect. While this would be of lesser importance in the clinic, this is a well-known limitation in preclinical mouse studies where the tumor size is more comparable with the image spatial resolution. For these reasons, the relationship between IHC and γ-counting is more informative. The results still need to be interpreted carefully, however, (i) only a limited sample number was included in this analysis, (ii) for γ-counting, the full excised tumor was analyzed, for IHC this was a single slide only; thus, tumor heterogeneity was not considered by the IHC analysis, and (iii) two tumor models were pooled for this analysis. The differences of the MKN-45 and HeLa tumor in regard to perfusion, necrosis, or stroma may also influence the results. In light of these limitations, the correspondence observed between IHC and CD8 quantitation with the PET tracer is encouraging.

In the MKN-45 or HeLA tumor–bearing humanized mice, ^{89}Zr-Df-IAB22M2C showed a favorable biodistribution, where it selectively accumulated in the tumor tissue, in lymphatic tissues, and in the clearance organs. The Mb had a very fast clearance from the blood, resulting in a high sensitivity with low background signals at 40 hours, which are desirable properties for PET imaging (16). Thus, the pharmacokinetic of the anti-CD8 Mb is favorable for PET imaging and overcomes limitations observed with full-length antibodies, which were previously used to image various T-cell epitopes such as CD3, CD4, CD25, or CD45 (30). Adverse events and infusion-related effects were not observed throughout the course of both preclinical studies, which is in-line with recent published clinical results (19). Liver uptake was observed for the Mb due to its hepatobiliary clearance. Although it is conceivable that this could affect the detection of CD8 cells in clearance organs, a recent publication from Pandit-Taskar and colleagues showed that the detection of tracer uptake in human liver tumors is feasible (19).

On the basis of our results, we conclude, that the anti-CD8 Mb ^{89}Zr-Df-IAB22M2C has a high potential to visualize and quantify CD8$^+$ T-cell infiltrates upon mono and combination cancer immunotherapy in primary lesions, metastasis, and malignant lymphoid tissues of patients with cancer. Whole-body PET imaging in the clinic offers the advantage of not being limited to the characterization of only one single tumor lesion, which is the often the case for biomarker analysis on tumor biopsies. IHC on needle biopsies are known to be affected by high rates of sampling errors, due to heterogeneity in the TME.

Alternative tracers that target CD8$^+$ T cells such as nanobodies have been described in preclinical studies and were able to monitor CD8$^+$ T-cell infiltrates following anti-CTLA-4 mAb treatment (27). However, a clinical application of these nanobodies to image CD8 in humans has not been reported to date (27). Besides targeting of the surface marker CD8, there are other PET tracers in clinical development that aim to target upregulated pathways in activated T cells (31, 32). However, it is conceivable that in the complex TME these pathways might also be upregulated in tumor cells or other immune cells as well, and therefore limit the ability of these probes to differentiate between activated immune cells and tumor cells based on PET imaging. Imaging T-cell activation through granzyme B, using a peptide-based tracer (28, 30), has the potential to provide complementary data to CD8 imaging, generating information directly related to the activation state of T cells. The peptide was used in syngeneic murine models during anti-CTLA-4 and anti-PD-1 therapy and was able to distinguish between responders and nonresponders (33, 34). Clinical evaluation in patients with cancer in the future will confirm whether imaging granzyme B is a feasible strategy in humans to monitor cancer immunotherapy. Radiolabeled IL2 with ^{99m}Tc or ^{18}F was also tested as a tracer in human patients with melanoma for scintigraphy (35, 36), but it was not confirmed that the IL2 tracer is able to monitor response to CPI treatment.

An additional imaging strategy in immune-oncology is the successful clinical application of radiolabeled antibodies against PD-1 (nivolumab) and PD-L1 (atezolizumab), as well as a PD-1-specific adnectin (37, 38). Clinical PET imaging with radiolabeled anti-PD-L1 full-length mAb enabled the identification of possible responders to PD-L1 therapy (37). Of note, the targeting of PD-L1 is not specific to immune cells as PD-L1 is also expressed by tumor cells, and immune cells such as macrophages, plus other cells in the TME (such as tumor stroma; ref. 39). The validity of PD-L1 in the TME as a predictive biomarker of response to immunotherapy is still controversial (40). In addition, the use of a full-length antibody as an imaging agent for diagnostic purposes is undesirable, due to the potential immunogenicity and long plasma half-life, which results in a high background signal and nonoptimal tumor uptake (16). More tracers that target PD-1 or PD-L1 are currently under preclinical development, and will reveal in the future whether differences between cancer immunotherapy combination partners can be observed, and whether these differences correlate with antitumoral efficacy (18, 41–43).

We present a preclinical application of a humanized, radiolabeled CD8-specific Mb, which is currently in clinical development (19), in two different tumor models in humanized mice. In separate cancer immunotherapy settings with immune-activating, tumor-associated antigen-specific mono- and combination therapies, the anti-CD8-Mb ^{89}Zr-Df-IAB22M2C Mb is able to differentiate varying levels of intratumoral CD8$^+$ T-cell infiltrates. The results show that PET imaging of CD8 T-lymphocyte infiltration in tumor lesions is a viable approach to monitor response to cancer immunotherapy.

Disclosure of Potential Conflicts of Interest

C.M Griessinger is a principal scientist (paid consultant) at Roche. T. Olafsen is a consultant (paid consultant) at and has ownership interest (including patents) in ImaginAb Inc. A. Mascioni is director of research (paid consultant) at and has

ownership interest (including patents) in ImaginAb. M. Torgov is a consultant (paid consultant) at Imaginab. T.K. Nayak is an employee (paid consultant) at Roche. M. Amann is a principal scientist (paid consultant) at Roche. P.L.B. Mohan is a senior research associate (paid consultant). V.G Nicolini is an employee (paid consultant) at Roche. J. Sam is a principal scientist and research group leader (paid consultant), and has ownership interest (including patents) in F. Hoffmann La Roche AG (WO 2017/118675). C. Claus is employed as a senior scientist (paid consultant) at Roche Innovation Center Zurich (part of pRED Hoffmann La Roche) and has ownership interest (including patents) in WO2016075278, WO2018114754, and WO2018114748 held/submitted by F. Hoffmann La Roche AG that cover tumor-targeted-4-1BBLs and their combination therapies. C. Ferrara is employed as a principal senior scientist (paid consultant) at Roche Innovation Center Zurich (part of pRED Hoffmann La Roche) and has ownership interest (including patents) in WO2016075278, WO2018114754, and WO2018114748 held/submitted by F. Hoffmann La Roche AG that cover tumor-targeted 4-1BBLs and their combination therapies. P. Brünker is a senior principal scientist (paid consultant) at Roche Innovation Center Zurich, Roche Pharma Research and Early Development. M. Bacac is a cancer immunotherapy-2 department head (paid consultant) at Roche. P. Umana is head cancer immunotherapy discovery (paid consultant) at and has ownership interest (including patents) in Roche. D. Rüttinger is global head early clinical development oncology (paid consultant) at, reports receiving a commercial research grant from, and has ownership interest (including patents) in Roche. I.A. Wilson is a CEO (paid consultant) at ImaginAb Inc. C. Klein is department head (paid consultant) and data manager at and has ownership interest (including patents) in Roche. J.J.L. Tessier is head of clinical imaging (paid consultant) at Roche pRED Oncology. No potential conflicts of interest were disclosed by the other authors.

Authors' Contributions

Conception and design: C.M. Griessinger, J.M. Romero, T.K. Nayak, M. Pincha, M. Amann, J. Sam, M. Bacac, P. Umana, D. Rüttinger, I.A. Wilson, J. Gudas, C. Klein, J.J.L. Tessier

Development of methodology: Z.K. Jiang, J.M. Romero, F. Marchioni, D. Satpayev, C. Lee, T.K. Nayak, M. Pincha, M. Amann, J. Sam, C. Klein, J.J.L. Tessier

Acquisition of data (provided animals, acquired and managed patients, provided facilities, etc.): T. Olafsen, Z.K. Jiang, C. Zamilpa, F. Jia, F. Marchioni, D. Satpayev, C. Lee, M. Pincha, P.L.B. Mohan, M. Richard, V.G. Nicolini

Analysis and interpretation of data (e.g., statistical analysis, biostatistics, computational analysis): C.M. Griessinger, Z.K. Jiang, C. Zamilpa, F. Marchioni, D. Satpayev, C. Lee, T.K. Nayak, M. Pincha, P.L.B. Mohan, V.G. Nicolini, D. Rüttinger, I.A. Wilson, J. Gudas, J.J.L. Tessier

Writing, review, and/or revision of the manuscript: C.M. Griessinger, T. Olafsen, A. Mascioni, F. Jia, M. Torgov, T.K. Nayak, M. Pincha, V.G. Nicolini, J. Sam, C. Claus, C. Ferrara, P. Brünker, M. Bacac, P. Umana, D. Rüttinger, I.A. Wilson, C. Klein, J.J.L. Tessier

Administrative, technical, or material support (i.e., reporting or organizing data, constructing databases): A. Mascioni, C. Zamilpa, D. Satpayev, P.L.B. Mohan, C. Claus, C. Ferrara, P. Brünker, J. Gudas, J.J.L. Tessier

Study supervision: D. Satpayev, M. Bacac, D. Rüttinger, J. Gudas, J.J.L. Tessier

Other (implantation of tumors, radiolabeling of PET tracers, injection or tracer via tail vein, PET/CT of animals, post-imaging necropsy and bio distribution, and autoradiography of tumors): C. Zamilpa

Other (responsible for methodology of the production of the imaging probe that was used in this study): M. Torgov

Other (generation of the study materials): G. Zhang

Acknowledgments

We would like to express special thanks of gratitude to Jean Gudas for her contribution to this project. We also thank Timothy J. Seabrook for his support. The presented studies were funded by ImaginAb Inc. and Roche.

The costs of publication of this article were defrayed in part by the payment of page charges. This article must therefore be hereby marked *advertisement* in accordance with 18 U.S.C. Section 1734 solely to indicate this fact.

Received October 18, 2019; revised February 21, 2020; accepted May 11, 2020; published first May 14, 2020.

References

1. Topalian SL, Taube JM, Anders RA, Pardoll DM. Mechanism-driven biomarkers to guide immune checkpoint blockade in cancer therapy. Nat Rev Cancer 2016; 16:275–87.
2. Bacac M, Colombetti S, Herter S, Sam J, Perro M, Chen S, et al. CD20-TCB with obinutuzumab pretreatment as next-generation treatment of hematologic malignancies. Clin Cancer Res 2018;24:4785–97.
3. Bacac M, Klein C, Umana P. CEA TCB: a novel head-to-tail 2:1 T cell bispecific antibody for treatment of CEA-positive solid tumors. Oncoimmunology 2016;5: e1203498.
4. Bacac M, Fauti T, Sam J, Colombetti S, Weinzierl T, Ouaret D, et al. A novel carcinoembryonic antigen T-Cell bispecific antibody (CEA TCB) for the treatment of solid tumors. Clin Cancer Res 2016;22:3286–97.
5. Lehmann S, Perera R, Grimm HP, Sam J, Colombetti S, Fauti T, et al. *In vivo* fluorescence imaging of the activity of CEA TCB, a novel T-cell bispecific antibody, reveals highly specific tumor targeting and fast induction of T-cell-mediated tumor killing. Clin Cancer Res 2016;22:4417–27.
6. Hammarstrom S. The carcinoembryonic antigen (CEA) family: structures, suggested functions and expression in normal and malignant tissues. Semin Cancer Biol 1999;9:67–81.
7. Leamon CP, Low PS. Folate-mediated targeting: from diagnostics to drug and gene delivery. Drug Discov Today 2001;6:44–51.
8. Weitman SD, Lark RH, Coney LR, Fort DW, Frasca V, Zurawski VR Jr, et al. Distribution of the folate receptor GP38 in normal and malignant cell lines and tissues. Cancer Res 1992;52:3396–401.
9. Schlothauer T, Herter S, Koller CF, Grau-Richards S, Steinhart V, Spick C, et al. Novel human IgG1 and IgG4 Fc-engineered antibodies with completely abolished immune effector functions. Protein Eng Des Sel 2016;29:457–66.
10. Kawalekar OU, RS OC, Fraietta JA, Guo L, McGettigan SE, Posey AD Jr, et al. Distinct signaling of coreceptors regulates specific metabolism pathways and impacts memory development in CAR T cells. Immunity 2016;44:712.
11. Melero I, Shuford WW, Newby SA, Aruffo A, Ledbetter JA, Hellstrom KE, et al. Monoclonal antibodies against the 4-1BB T-cell activation molecule eradicate established tumors. Nat Med 1997;3:682–5.
12. Lovdal T, Andersen E, Brech A, Berg T. Fc receptor mediated endocytosis of small soluble immunoglobulin G immune complexes in Kupffer and endothelial cells from rat liver. J Cell Sci 2000;113:3255–66.
13. Segal NH, Logan TF, Hodi FS, McDermott D, Melero I, Hamid O, et al. Results from an integrated safety analysis of urelumab, an agonist anti-CD137 monoclonal antibody. Clin Cancer Res 2017;23:1929–36.
14. Claus C, Ferrara C, Xu W, Sam J, Lang S, Uhlenbrock F, et al. Tumor-targeted 4-1BB agonists for combination with T cell bispecific antibodies as off-the-shelf therapy. Sci Transl Med 2019;11:eaav5989. DOI: 10.1126/scitranslmed.aav5989.
15. Drent E, Poels R, Ruiter R, van de Donk N, Zweegman S, Yuan H, et al. Combined CD28 and 4-1BB costimulation potentiates affinity-tuned chimeric antigen receptor-engineered T cells. Clin Cancer Res 2019;25:4014–25.
16. Freise AC, Wu AM. *In vivo* imaging with antibodies and engineered fragments. Mol Immunol 2015;67:142–52.
17. Donnelly DJ, Smith RA, Morin P, Lipovsek D, Gokemeijer J, Cohen D, et al. Synthesis and biologic evaluation of a Novel (18)F-labeled adnectin as a PET radioligand for imaging PD-L1 expression. J Nucl Med 2018;59: 529–35.
18. Maute RL, Gordon SR, Mayer AT, McCracken MN, Natarajan A, Ring NG, et al. Engineering high-affinity PD-1 variants for optimized immunotherapy and immuno-PET imaging. Proc Natl Acad Sci U S A 2015;112:E6506–14.
19. Pandit-Taskar N, Postow M, Hellmann M, Harding J, Barker C, O'Donoghue J, et al. First-in-human imaging with (89)Zr-Df-IAB22M2C anti-CD8 minibody in patients with solid malignancies: preliminary pharmacokinetics, biodistribution, and lesion targeting. J Nucl Med 2020;61:512–9.
20. Loening AM, Gambhir SS. AMIDE: a free software tool for multimodality medical image analysis. Mol Imaging 2003;2:131–7.
21. Tavare R, Escuin-Ordinas H, Mok S, McCracken MN, Zettlitz KA, Salazar FB, et al. An effective immuno-PET imaging method to monitor CD8-dependent responses to immunotherapy. Cancer Res 2016;76:73–82.
22. Rongvaux A, Willinger T, Martinek J, Strowig T, Gearty SV, Teichmann LL, et al. Development and function of human innate immune cells in a humanized mouse model. Nat Biotechnol 2014;32:364–72.

23. Yong KSM, Her Z, Chen Q. Humanized mice as unique tools for human-specific studies. Arch Immunol Ther Exp 2018;66:245–66.
24. Zumwalde NA, Gumperz JE. Modeling human antitumor responses in vivo using umbilical cord blood-engrafted mice. Front Immunol 2018;9:54.
25. Morton JJ, Bird G, Refaeli Y, Jimeno A. Humanized mouse xenograft models: narrowing the tumor-microenvironment gap. Cancer Res 2016;76:6153–8.
26. Sanmamed MF, Rodriguez I, Schalper KA, Onate C, Azpilikueta A, Rodriguez-Ruiz ME, et al. Nivolumab and urelumab enhance antitumor activity of human T lymphocytes engrafted in Rag2-/-IL2Rγnull immunodeficient mice. Cancer Res 2015;75:3466–78.
27. Rashidian M, Ingram JR, Dougan M, Dongre A, Whang KA, LeGall C, et al. Predicting the response to CTLA-4 blockade by longitudinal noninvasive monitoring of CD8 T cells. J Exp Med 2017;214:2243–55.
28. Seo JW, Tavare R, Mahakian LM, Silvestrini MT, Tam S, Ingham ES, et al. CD8(+) T-cell density imaging with (64)Cu-Labeled Cys-Diabody informs immunotherapy protocols. Clin Cancer Res 2018;24:4976–87.
29. Tavare R, McCracken MN, Zettlitz KA, Knowles SM, Salazar FB, Olafsen T, et al. Engineered antibody fragments for immuno-PET imaging of endogenous CD8+ T cells in vivo. Proc Natl Acad Sci U S A 2014;111:1108–13.
30. Malviya G, Galli F, Sonni I, Signore A. Imaging T-lymphocytes in inflammatory diseases: a nuclear medicine approach. Q J Nucl Med Mol Imaging 2014;58:237–57.
31. Namavari M, Chang YF, Kusler B, Yaghoubi S, Mitchell BS, Gambhir SS. Synthesis of 2'-deoxy-2'-[18F]fluoro-9-beta-D-arabinofuranosylguanine: a novel agent for imaging T-cell activation with PET. Mol Imaging Biol 2011;13:812–8.
32. Ronald JA, Kim BS, Gowrishankar G, Namavari M, Alam IS, D'Souza A, et al. A PET imaging strategy to visualize activated T cells in acute graft-versus-host disease elicited by allogenic hematopoietic cell transplant. Cancer Res 2017;77:2893–902.
33. Larimer BM, Bloch E, Nesti S, Austin EE, Wehrenberg-Klee E, Boland G, et al. The effectiveness of checkpoint inhibitor combinations and administration timing can be measured by granzyme B PET imaging. Clin Cancer Res 2018:11:7369–83.
34. Larimer BM, Wehrenberg-Klee E, Dubois F, Mehta A, Kalomeris T, Flaherty K, et al. Granzyme B PET imaging as a predictive biomarker of immunotherapy response. Cancer Res 2017;77:2318–27.
35. Signore A, Annovazzi A, Barone R, Bonanno E, D'Alessandria C, Chianelli M, et al. 99mTc-interleukin-2 scintigraphy as a potential tool for evaluating tumor-infiltrating lymphocytes in melanoma lesions: a validation study. J Nucl Med 2004;45:1647–52.
36. Hartimath SV, Draghiciu O, van de Wall S, Manuelli V, Dierckx RA, Nijman HW, et al. Noninvasive monitoring of cancer therapy induced activated T cells using [(18)F]FB-IL-2 PET imaging. Oncoimmunology 2017;6:e1248014.
37. Bensch F, van der Veen EL, Lub-de Hooge MN, Jorritsma-Smit A, Boellaard R, Kok IC, et al. (89)Zr-atezolizumab imaging as a non-invasive approach to assess clinical response to PD-L1 blockade in cancer. Nat Med 2018;24:1852–8.
38. Niemeijer AN, Leung D, Huisman MC, Bahce I, Hoekstra OS, van Dongen G, et al. Whole body PD-1 and PD-L1 positron emission tomography in patients with non-small-cell lung cancer. Nat Commun 2018;9:4664.
39. Liu Y, Zugazagoitia J, Ahmed FS, Henick BS, Gettinger S, Herbst RS, et al. Immune cell PD-L1 co-localizes with macrophages and is associated with outcome in PD-1 pathway blockade therapy. Clin Cancer Res 2019;26:970–77.
40. Patel SP, Kurzrock R. PD-L1 expression as a predictive biomarker in cancer immunotherapy. Mol Cancer Ther 2015;14:847–56.
41. Broos K, Keyaerts M, Lecocq Q, Renmans D, Nguyen T, Escors D, et al. Non-invasive assessment of murine PD-L1 levels in syngeneic tumor models by nuclear imaging with nanobody tracers. Oncotarget 2017;8:41932–46.
42. Kumar D, Lisok A, Dahmane E, McCoy M, Shelake S, Chatterjee S, et al. Peptide-based PET quantifies target engagement of PD-L1 therapeutics. J Clin Invest 2019;129:616–30.
43. Ingram JR, Dougan M, Rashidian M, Knoll M, Keliher EJ, Garrett S, et al. PD-L1 is an activation-independent marker of brown adipocytes. Nat Commun 2017;8:647.